# Characterization of the nonlinear behavior of nodular graphite cast iron via inverse identification: Analysis of biaxial tests

Zvonimir Tomicevic, Janos Kodvanj, François Hild

# Characterization of the nonlinear behavior of nodular graphite cast iron via inverse identification

## Analysis of biaxial tests

Zvonimir Tomičević[a,b], Janoš Kodvanj[a], François Hild[b]

[a]*Department of Engineering Mechanics, Faculty of Mechanical Engineering and Naval Architecture, University of Zagreb, Ivana Lučića 5, 10000 Zagreb Croatia*
[b]*LMT-Cachan, ENS Cachan/CNRS/University Paris-Saclay, 61 avenue du Président Wilson, 94235 Cachan Cedex, France*

**Abstract**

In this paper the nonlinear behavior of nodular graphite cast iron is investigated under in-plane biaxial loading regimes. Multiaxial experiments enable a wide variety of loading paths to be investigated. In the presented study two loading histories are proposed, namely, equibiaxial and "snail" loading paths corresponding to proportional and nonproportional regimes. The center gauge zone of the testing cruciform specimen is observed. Mean strain fluctuations are measured and presented in order to determine the material response for the prescribed biaxial loading paths. For the equibiaxial and snail loading histories finite element model updating will couple 2D-DIC measurements with 3D-FE analyses to calibrate material parameters describing elasticity, isotropic or kinematic hardening.

*Keywords:* Digital Image Correlation, Full-field measurements, In-plane biaxial experiments, Nonlinear constitutive models, Material parameter identification, Proportional and nonproportional loading.

## 1. Introduction

During their exploitation the majority of engineering structures is subjected to complex loading regimes (*e.g.,* aeronautical, astronautical, automotive, chemical, power generation, oil, and transportation industries). The extensive use of engineering structures over such a wide range of applications has generated extraordinary interest in the material behavior and fatigue durability under multiaxial loading conditions. Specifically, the technical areas of interest include strength of materials under multiaxial loading conditions, multiaxial deformation and fatigue of materials, and development of multiaxial experimental capabilities to test materials under controlled prototypical loading conditions. To describe these loading regimes in more reliable manners multiaxial experiments started to be conducted in the last three decades [1]. With the development of multiaxial testing machines (biaxial, triaxial, hexapod) a new era of experiments was opened thanks to the possibility of prescribing a wide range of loading histories [2, 3]. The results of multiaxial tests are important, in particular, for the characterization of the material properties and the development of constitutive laws that can be used for predictive purposes (*e.g.,* in fatigue).

Furthermore, identification procedures have been developed to explicitly deal with full-fields [4, 5, 6]. In terms of kinematic fields measured via digital image correlation (DIC), new procedures are also considered. For instance, integrated techniques [9] can be introduced in which the material parameters and their kinematic sensitivities are directly accounted for. This type of procedure enables arbitrary discretizations to be considered in the investigated area without increase of standard displacement resolution as expected

in standard and global DIC approaches [10]. Second, when dealing with multiaxial tests, 2D-DIC may yield spurious measurements due to out-of-plane motions. One way of circumventing this limitation is to resort to stereoDIC on a more regular basis [6, 7, 8].

The work presented in this paper follows on the previous study on the same material subjected to uniaxial tests [11] to probe nonlinear models thanks to combined kinematic and static gaps associated with the finite element model updating (*i.e.,* FEMU-UF) technique. The present study deploys FEMU on more complex loading histories, namely, biaxial tests are considered. Since in-plane biaxial experiments give an opportunity to apply a wide variety of loading histories two different biaxial loading paths (*i.e.,* equibiaxial and "snail") will be used. The proposed work consists of two parts. First, the proportional and nonproportional loading histories will be introduced. From the measured displacement/strain fields the mean strain history will be extracted in order to discuss the material response to the various histories. The second part will consider the identification of elastoplastic (*i.e.,* isotropic and kinematic hardening) parameters via the FEMU-UF procedure for the two applied loading histories. The identification procedure consists of coupling 2D-DIC measurements with 3D-FE models.

## 2. In-plane biaxial experimental protocol

### *2.1. Triaxial testing machine*

Biaxial tests were conducted on the triaxial servohydraulic machine ASTREE (Figure 1). The loading frame of the machine is composed of a base, four vertical columns and a mobile crosshead. Among the six available ac-

tuators, the four horizontal ones are used for the reported tests. They have a load capacity of 100 kN and a 250-mm stroke range. Such a setup has already been used for monotonic as well as cyclic biaxial tests [12, 13, 2, 3]. For protection against potential side and twist forces applied by the other actuators, additional hydraulic bearings are installed in front of each actuator. The hydraulic power is supplied by stations that can generate a 600 l/min maximum flow rate.

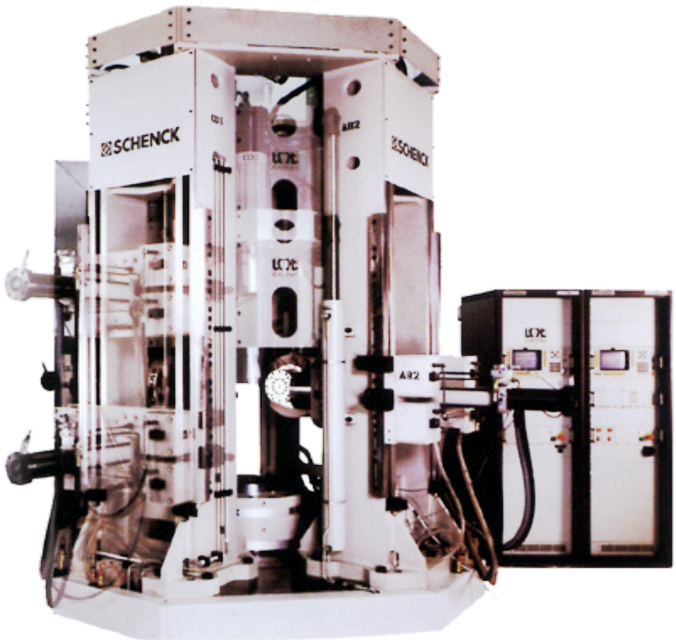


Figure 1: Triaxial testing machine ASTREE

The testing machine is equipped with a highly versatile digital controller (Instron 8800) and by its related interface software (Consol 8.2 build 133). This environment allows each actuator to be controlled independently, but also to perform virtually any closed-loop control using linear combinations of the different input signals. For the biaxial tests reported hereafter, a "modal

control" type is used. It is based on a relationship between the two forces $F_1$ and $F_2$ of two opposite actuators along the same load axis ($X$, $Y$ or $Z$) to control both the mean force $(F_1 + F_2)/2$ and the force difference $(F_1 - F_2)/2$. Consequently, the loading is "balanced" between the two actuators if the prescribed force difference cancels out.

### *2.2. In-plane cruciform specimen*

The tested specimens for biaxial experiments are maltese crosses thinned in the central part with non homogeneous strain/stress fields. The sample was designed in order to allow for crack initiation in biaxial conditions in the central part. The prime design of a maltese cross shaped specimen was tested in this machine [12]. Improvements were implemented on the sample shape used herein following additional studies [2]:

- First, elastic calculations were performed using the damage equivalent stress to ensure that higher stress levels appear in the center of specimen rather than in the fillets between the arms. This criterion takes into account the stress triaxiality in the design.

- Second, the theoretical location of the first initiated crack is checked via a damage post-processing (DAMAGE_2005) using a two-scale damage model [14].

The optimized geometry is shown in Figure 2. The global size of the sample equals $274 \times 274$ mm$^2$. The thickness at the center is equal to 1 mm and it is gradually increasing to 5 mm out of the gauge zone, which creates a calotte with of circular base 30 mm in diameter. The dimension of the fillets of the

gripping arms is 12 mm. This geometry was originally designed for positive load ratios [2].

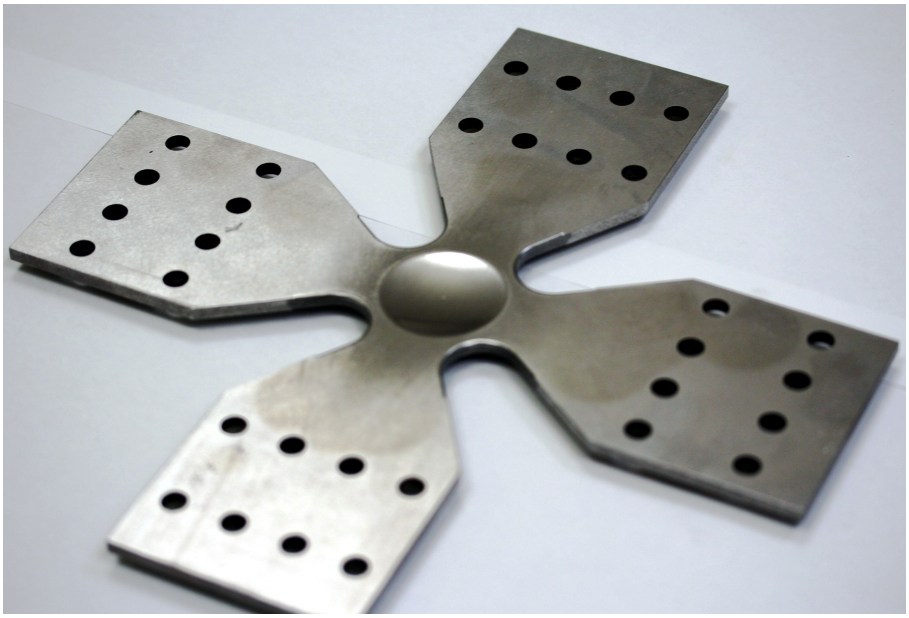

Figure 2: Maltese cross-shaped specimen designed for in-plane biaxial experiments

*2.3. Optical setup*

Since the geometry of the specimen is complex, the natural choice is to use full-field measurements to have access to the displacement/strain distributions during the experiment. The experiments are carried out in the horizontal plane (Figure 3). The thinned part of the cross-shaped specimen was observed from the bottom side (Figure 3(a)) for which the camera monitors the whole gauge zone. Images were taken with a CCD camera (*Dalsa*, 12-bit digitization) and a telecentric lens with a magnification $\times 4$ (Figure 3(b)). The picture definition is $1024 \times 1024$ pixels with a physical pixel size of 48 $\mu$m (Figure 3(c)). The proposed observation scale was taken

since it was important to acquire stress-free edges in order to correctly position the mesh for DIC analyses with respect to the sample geometry. A fine speckle pattern was printed with an airbrush (*i.e.,* ink jet printer, see Figure 3(c)).

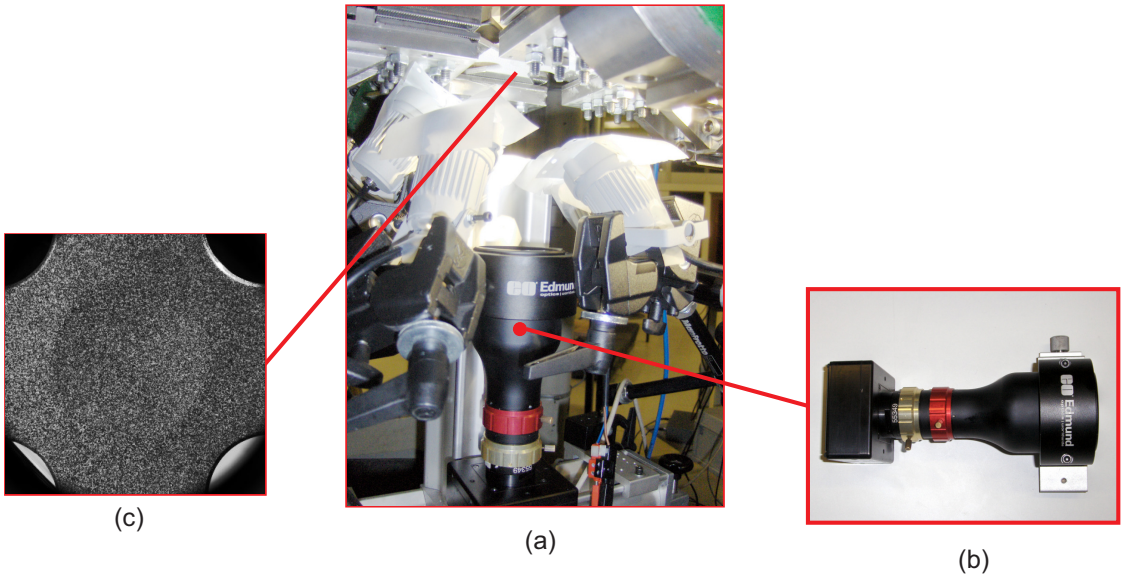


Figure 3: Experimental setup. (a) Optical setup, (b) CCD *Dalsa* camera with telecentric lens (magnification $\times 4$), (c) macroscale image

### *2.4. Applied load histories*

Multiaxial experiments (*e.g.,* in-plane biaxial tests) allow for a wide range of loading paths without any protocol change (especially no geometry modification), which is an important parameter [13, 2]. In the present investigation two different histories are considered, namely, equibiaxial and "snail" loading paths.

The equibiaxial loading history (Figure 4(a)) corresponds to a "proportional" in-plane biaxial loading where both perpendicular axes are loaded and

unloaded at the same level. The "snail" regime (Figure 4(b)) first (un)loads the specimen in the 1-direction while the load in the 2-direction is constant. In the next (un)loading step the specimen is (un)loaded in direction 2 while the load is constant in direction 1. Both loading paths were cycled with increasing maximum force (*i.e.,* $F^{\max}$) in the loading part while the minimum force (*i.e.,* $F^{\min}$) was constant.

Before conducting in-plane biaxial experiments an FE analysis is performed to determine the increase of peak forces for each cycle. Considering the two planes of symmetry, a quarter of the cross-shaped sample is used for the FE model. A Ludwik's isotropic hardening model is chosen with the elastoplastic parameters obtained from a uniaxial experiment [11]. The results obtained with the FE analysis showed that plastic strains occur when the applied load is greater than 30 kN. For both loading histories, the first 3 steps of loading and unloading were chosen with an increment of 10 kN, and then the increment was set to 7.5 kN.

The cyclic biaxial experiments were performed in a load controlled mode with a loading rate of 0.5 kN/s. To successfully associate each image to a point in the loading sequence the CCD camera is triggered by the load controller. Figure 5 shows the applied equibiaxial loading path with the corresponding image number. Images were captured for each (un)loading increment of 1 kN (*i.e.,* the acquisition rate equals 0.5 frames/s). During the seven loading/unloading sequences 594 images were shot. The specimen broke for a load level of 59 kN (Figure 5).

Two experiments with the snail path are carried out with different boundary conditions. First, the snail experiment (Figure 6(a)) was fully load-

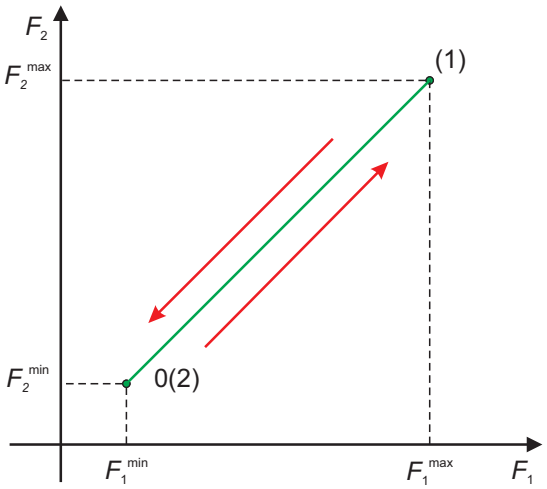


(a) Equibiaxial loading path

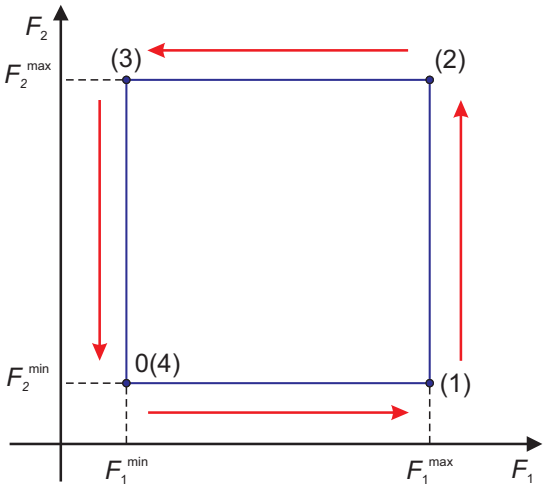


(b) "Snail" loading path

Figure 4: One cycle for (a) equibiaxial and (b) snail loading histories. Equibiaxial loading consists of two (*i.e.*, (1)-(2)) characteristic points while the snail history has four (*i.e.*, (1)-(2)-(3)-(4))

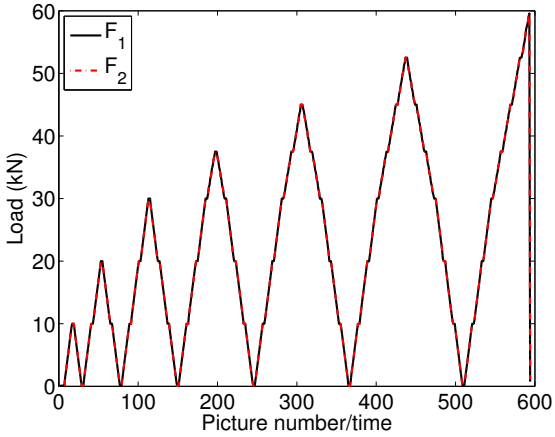


Figure 5: Equibiaxial loading regime. Applied load level with respect to number of pictures

controlled. The experiment was performed with the same parameters as previously mentioned for the equibiaxial loading regime. During the seven loading cycles 897 images were acquired, and the sample broke for a load level of 56 kN. The second snail experiment (Figure 6(b)) used a hybrid loading history (*i.e.,* when specimen is (un)loaded in direction 1 with a force control, the displacement of direction 2 is constant). Figure 6(b) shows a load relaxation for a constant displacement. From the measured load in both directions it is observed that the force in direction 2 (*i.e.,* $F_2$) leads to a higher decrease of load. The applied load rate was the same as in the previous experiment, while the acquisition rate was 40 frames/cycle. The specimen broke at the eighth loading cycle at a level of 52 kN. The reason why the nonproportional loading regime has the name snail lies in the the form of the loading path for the two loading directions (Figure 7).

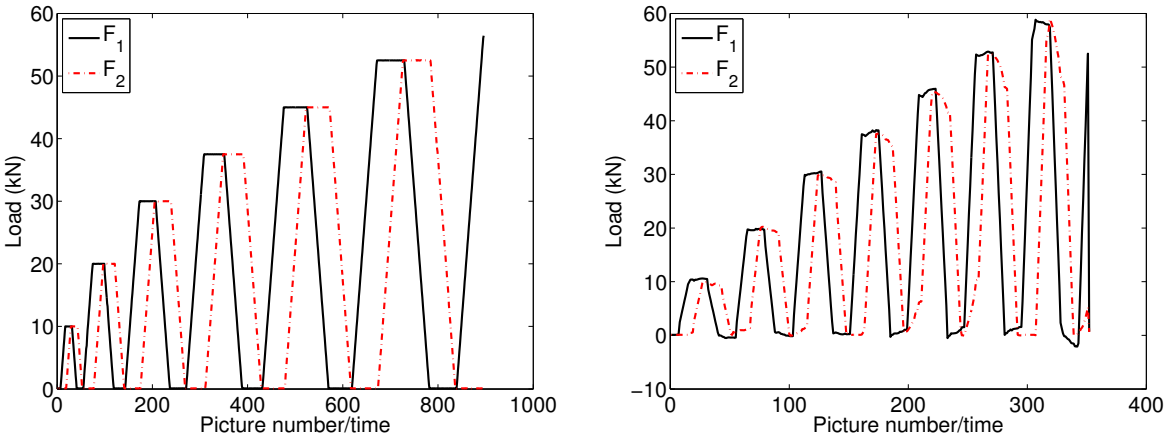


(a) Fully load controlled (b) Hybrid control

Figure 6: Snail loading paths. Applied load level with respect to number of images

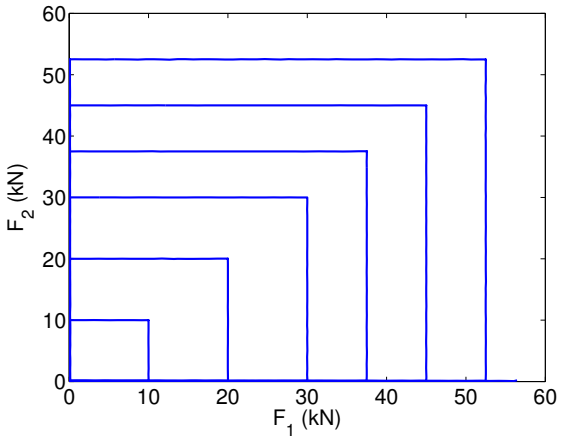


(a)

Figure 7: Measured load history for the load controlled snail test

## 3. Mean strain history

Even though the geometry of the specimen is complex and the central zone (*i.e.*, calotte) is thinned, the mean strain on the latter surface is evaluated. For the two loading histories an optical/virtual DIC strain gauge was applied (Figure 8). From the measured displacement via T3-DIC [15], the mean strain is extracted with a linear regression of the displacement components within the gauge. The latter was positioned in the center of the cruciform specimen with a size of $150 \times 150$ pixels (*i.e.*, $7.2 \times 7.2$ mm). The aim of this study is to compare the global strain fluctuations for the proposed in-plane biaxial loading regimes. Moreover, the material response for the imposed proportional and nonproportional loading histories will also be compared and discussed.

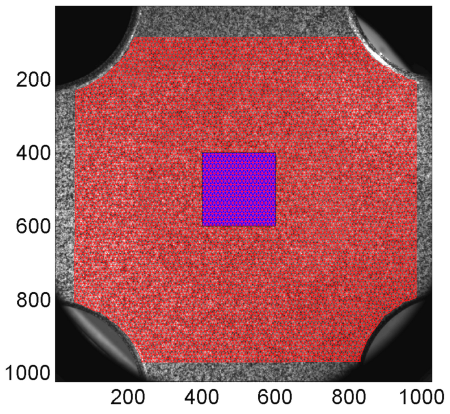


Figure 8: Optical DIC gauge depicted as a blue box over the T3 unstructured mesh with 10 pixel elements (red)

The equibiaxial loading regime is analyzed for the 594 acquired images. The measured strain components $\epsilon_{11}$ and $\epsilon_{22}$ in Figure 9(a) correspond to

the normal levels in the loading directions while $\epsilon_{12}$ denotes the shear strain component.

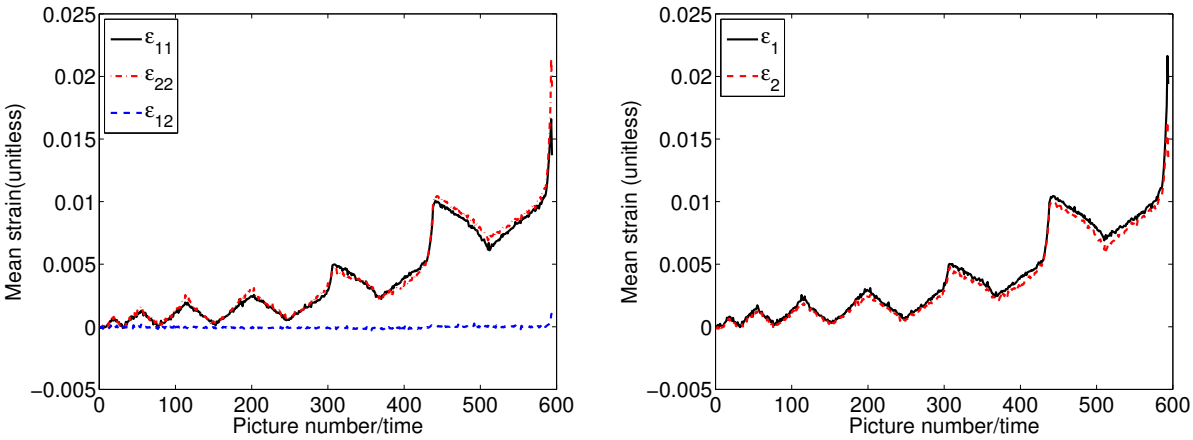


(a) (b)

Figure 9: Change of (a) $\epsilon_{11}$, $\epsilon_{22}$, $\epsilon_{12}$ and (b) $\epsilon_1$, $\epsilon_2$ during the equibiaxial test

From Figure 9(a) it is concluded that the strain components $\epsilon_{11}$ and $\epsilon_{22}$ exactly follow the same trend, which corresponds to an equibiaxial loading. Similarly, the eigen strains shown in Figure 9(b) coincide until the very end of the test. This results explains why small fluctuations of $\epsilon_{12}$ occur. In terms of eigen strain component $\epsilon_1$ and $\epsilon_2$, the experiment is fully proportional until cracks develop as opposed to the nonproportional loading regime of the snail test (Figure 10). Low levels of $\epsilon_{12}$ strains are also reported in Figure 9(a). During the whole experiment they are virtually constant since the sample is observed on a lower magnification scale. In comparison with uniaxial experiments where the maximum elongation was 4.5 % [11] it is lower for an equibiaxial loading regime (*i.e.,* 2.3 %). However it is worth remembering that the strain field is not uniform over an area where the thickness changes

(*i.e.*, thinned center part of the cross-shaped sample).

The same DIC strain gauge is considered for the analysis of fully load controlled and hybrid snail experiments (Figure 8). The results extracted with the optical strain gauge for the two snail histories show the same trend for the mean strain fluctuations. Hence, only mean strain components for fully load controlled test are presented. Figure 10(a) shows the strain history along the two loading axes. As opposed to the equibiaxial loading regime (Figure 9(a)) in the present case $\epsilon_{11}$ and $\epsilon_{22}$ follow completely different paths. As for the equibiaxial test case small fluctuations of the shear strain component $\epsilon_{12}$ are noted.

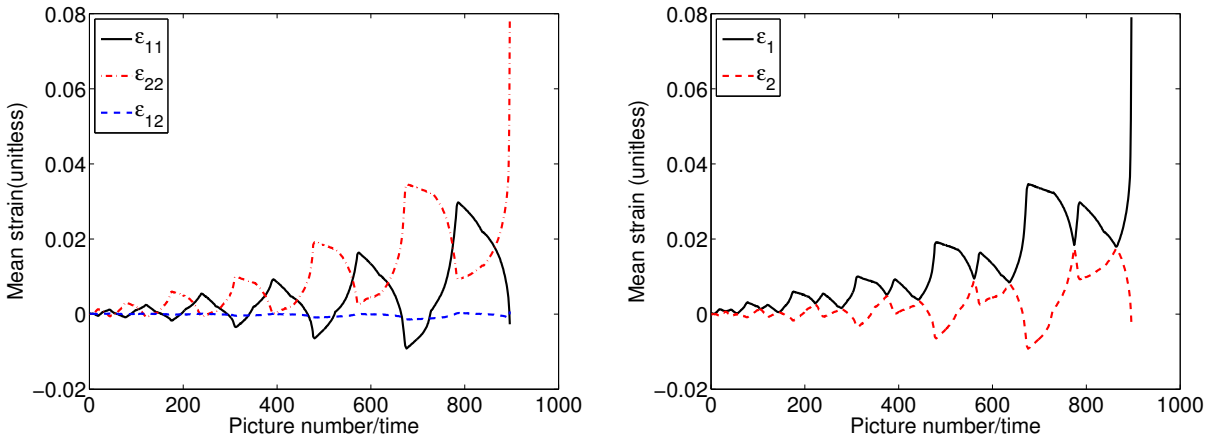


Figure 10: Change of (a) $\epsilon_{11}$, $\epsilon_{22}$, $\epsilon_{12}$ and (b) $\epsilon_1$, $\epsilon_2$ during the the fully load-controlled snail test

In the previous case when the mean eigen strains were presented (Figure 9(b)) it was noted how they coincided during virtually all the experiment. From Figure 10(b) it can be noted that this is not the case for nonproportional snail loading. From the measured data it is concluded that the material

is loaded in a completely different way. In the sequel elastoplastic parameters will be identified for the equibiaxial and snail loading regimes.

## 4. 3D-FEMU procedure using 2D-DIC measurements

The central part of the cross-shaped sample is observed during biaxial loading. The highest stress levels occur in its thinned gauge zone (*i.e.,* calotte). Since the sample has a complex geometry it is necessary to resort to a 3D-FE model even though 2D-DIC measurements are available. First, the 3D mesh is designed in the commercial (implicit) FE code Abaqus/Standard. From the model surface the nodes are extracted into a set that defines the 2D mesh that is imported in the T3-DIC code. The 2D mesh is adjusted and scaled to the macroscopic scale on the reference image of the tested sample.

The T3-DIC code provides the measured displacement fields. The in-plane nodal displacements on the boundary of the T3 mesh are extracted and prescribed to the 3D FE model. The same displacements are prescribed through the thickness along the edges. Since the radii of the cross-shaped specimen are traction-free during the test they were treated as such and displacements were not prescribed in that region. To save for computation time only one symmetry was applied with respect to the surface normal.

For each iteration of the FEMU-UF procedure [16, 11] the displacements of the surface nodes are extracted and compared with measured ones in the kinematic $\chi_u$ residual. The sum of reaction forces is obtained from the boundary nodes in the simulations. Reaction forces along both directions are gathered in one column vector. Differences of the measured and calculated

force vector is assessed in the static residual $\chi_F$. The initial parameters are taken from the identification results of uniaxial experiments. Hence, the identified elastoplastic parameters of the two loading histories will be compared with the total residual, $\chi^2_{tot}$, which is a weighted sum of $\chi^2_u$ and $\chi^2_F$ [11].

The constitutive postulates calibrated herein are built-in models in Abaqus/Standard. Isotropic elasticity is either coupled with nonlinear hardening (*i.e.,* Ludwik's law [17]) or nonlinear kinematic hardening (*i.e.,* Armstrong-Frederick's law [18]), see Appendix A. The identified parameters have their uncertainties evaluated by propagating the displacement and load uncertainties [16, 19, 11]. They are reported with the corresponding $\pm$ standard uncertainty.

## 5. Identification results for equibiaxial loading regime

### *5.1. Elastic parameters*

The identification of elastic parameters is carried out on the first two and a half cycles, which correspond to 104 pictures. The parameters used for the FE simulation in order to determine the load levels of the biaxial experiments differ from those identified via uniaxial tests [11]. Hence, the chosen maximum load level considered in the analysis of elastic parameters is equal to 20 kN. Before performing the identification over the whole series of images in the elastic region the measurement uncertainty is evaluated. Nine pictures were shot at the beginning of the experiment when the specimen was mounted and the load was constant (*i.e.,* $F_1 = F_2 \approx 0$). The standard displacement uncertainty is 0.02 pixel and the corresponding load resolution

equals 3.9 N.

Poisson's ratio and Young's modulus are identified via the FEMU-UF procedure. The initial values are chosen from the uniaxial experiment (Table 1). The identified values lead to a decrease of $\chi_u$ and $\chi_F$. Low displacement residuals between the measured and calculated displacement fields are reported even though a 3D model is run with displacements measured with 2D-DIC. Conversely, the load residual remains significantly higher than the resolution of the load cell. Since only a small part of the boundary of the FE model has traction-free edges, initial and identified values of the functional $\chi_u$ are close to the standard resolution. This does not allow for successfully identifying Poisson's ratio (Table 1). Another reason is related to the results of Figure 9(b), which show that the experiment is purely equibiaxial in the considered part of the test.

Table 1: Initial and identified elastic material parameter for equibiaxial experiment

| | E (GPa) | $\nu$ | $\chi_u$ | $\chi_F$ |
|---|---|---|---|---|
| Reference | 158 | 0.28 | 1.3 | 310 |
| FEMU-UF | 157±1 | 0.09±0.005 | 1.2 | 240 |

The second parameter identified with this procedure (*i.e.,* Young's modulus) yields a decrease of $\chi_F$ of 70 (Table 1) for the identified value (156 GPa). Figure 11 shows the comparison of initial and identified load levels in the two loading directions with respect to the measured data. Significant load fluctuations are noted at the beginning of the experiment (nine images where shot when the specimen was mounted and the applied load was $F_1 = F_2 \approx 0$ N).

They are due to measurement uncertainties and control errors. Further, at the end of unloading of the second cycle the load level does not reach 0 kN. These phenomena contribute to higher levels of the force residual $\chi_F$.

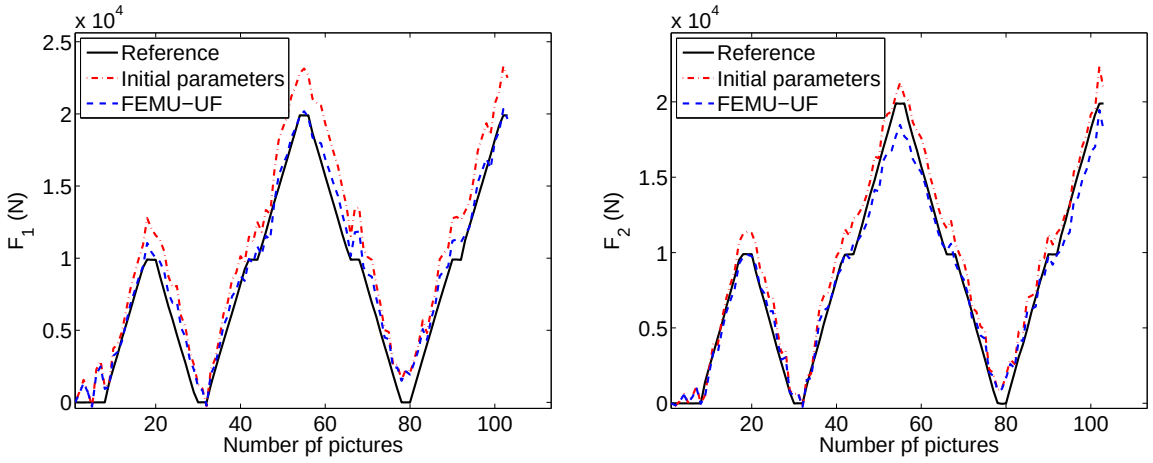


(a) Direction 1 (b) Direction 2

Figure 11: Comparison of measured force and sum of reaction forces computed with initial and identified elastic parameters

### *5.2. Isotropic and kinematic hardening parameters*

The first part of the identification of nonlinear material parameters will deal with isotropic hardening. In a second step kinematic hardening will be considered. The identification will be carried out with all images acquired during the equibiaxial experiment (*i.e.,* 594 pictures). The goal is to compare the identified parameters from the biaxial experiments with those determined from a monotonic uniaxial test [11], which are used as initial estimates.

*5.2.1. Ludwik's law*

Three material parameters (*i.e.*, $\sigma_y$, $K$ and $n$) describing Ludwik's model [11] are identified. The initial parameters are listed in Table 2. When they are introduced in the first iteration of the identification procedure the displacement residuals are equal to 2.8, while the force residual is equal to 1210. The equilibrium gap $\chi_F$ indicates that uniaxial material parameters are not suitable to describe the equibiaxial loading path (Figure 12).

The three identified values yield a decrease of the displacement residuals by 30% and by 40% for the force residuals (Table 2). Observing the load levels in both directions (Figure 12) the identified equibiaxial loading history better corresponds to the measured data. The unloading level of the last cycle does not describe properly the applied loading level. From this result, it can be concluded that kinematic hardening or damage phenomena may cause higher force residuals (*i.e.*, $\chi_F = 700$).

Table 2: Initial and identified Ludwik's parameters for an equibiaxial loading path

| | $E$ (GPa) | $\nu$ | $\sigma_Y$ (MPa) | $K$ (MPa) | $n$ | $\chi_u$ | $\chi_F$ |
|---|---|---|---|---|---|---|---|
| Reference | 157 | 0.28 | 207 | 1300 | 0.44 | 2.8 | 1210 |
| FEMU-UF | 157 | 0.28 | 226±1.5 | 1590±4 | 0.43±0.001 | 2.0 | 700 |

It is also necessary to emphasize that the identified load levels are better captured in the loading parts of the equibiaxial path. Similar trends were reported for the uniaxial test [11].

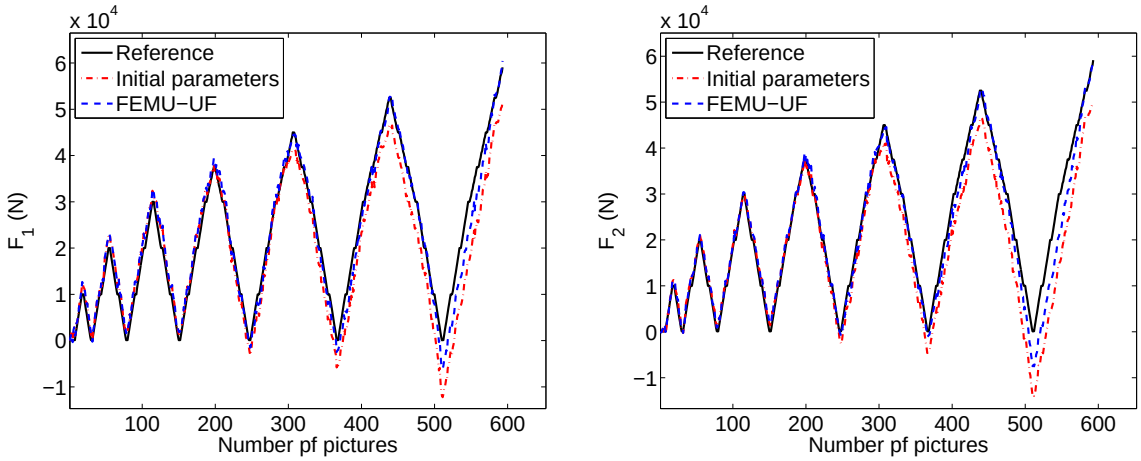


(a) Direction 1 (b) Direction 2

Figure 12: Comparison of measured force and sum of reaction forces computed with initial and identified material parameters for Ludwik's constitutive law

### *5.2.2. Armstrong-Frederick's law*

In the analysis of the elastoplastic behavior of cast iron under cyclic and uniaxial loading history [11] it was noted that kinematic hardening better described the cyclic response than isotropic hardening. For the same experimental data the identified parameters of Armstrong-Frederick's law yielded lower force residuals when compared with Ludwik's model. The same trend is reported for the equibiaxial loading regime (see Table 3). When observing the load residual $\chi_F$ for the two models (Tables 2 and 3) Armstrong-Frederick's results lead to a decrease of 250, so that the final level is only two times higher when compared with that obtained in elasticity.

As in the previous case (*i.e.,* identification of isotropic hardening parameters) the initial values of the sought parameters were taken from uniaxial data [11]. The identified parameters are shown in Table 3. A slight decrease

Table 3: Initial and identified Armstrong-Frederick's parameters via FEMU-UF for an equibiaxial loading path

| | $E$ (GPa) | $\nu$ | $\sigma_Y$ (MPa) | $C$ (GPa) | $\gamma$ | $\chi_u$ | $\chi_F$ |
|---|---|---|---|---|---|---|---|
| Reference | 157 | 0.28 | 222 | 27 | 107 | 2.1 | 1090 |
| FEMU-UF | 157 | 0.28 | 252±0.1 | 37±0.04 | 100±1 | 1.7 | 450 |

by 30 MPa of the yield stress is noted. The identified hardening modulus $C$ increases by 27 % while $\gamma$ decreases by 6 %. As mentioned previously the identified parameters decrease significantly the force residuals while $\chi_u$ decreases also. The displacement residuals are about 1.5 times the level observed in the elastic identification step.

Figure 13 shows the change of the calculated sum of reaction forces in the two loading direction when the initial and identified parameters are considered. They are compared with the measured load corresponding to each acquired picture. When using Armstrong-Frederick's law the unloading parts of the history are better captured then with Ludwik's law. When comparing parameters describing kinematic hardening determined from equibiaxial and uniaxial experiments, differences are noted. This leads us to conclude that uniaxial tests do not necessarily provide kinematic hardening parameters to describe credibly more complex loading regimes.

## 6. Identification results for snail loading histories

The results presented in the sequel correspond to a nonproportional loading regime (see Section 2.4).

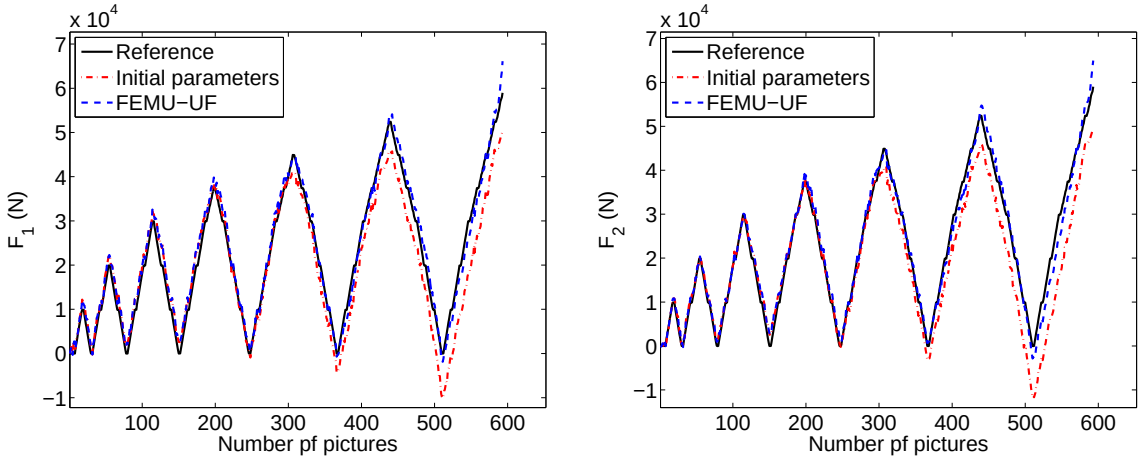


(a) Direction 1 (b) Direction 2

Figure 13: Comparison of measured force and sum of reaction forces computed with initial and identified parameters for Armstrong-Frederick' constitutive law

### *6.1. Validation of elastic parameters*

In the following, the two snail tests will be analyzed via FEMU-UF. Before discussing the results, the measurement uncertainty is calculated from 10 images when the load was not applied. From the standard resolutions (Table 4) it is noted that the displacement resolution for the load controlled test case is 50% lower than for the hybrid one. It is believed that the main difference is due to the random texture. The identification of the elastic properties is carried out on the first two cycles. The fully load-controlled test case consisted of 144 pictures while the hybrid one included 101 pictures.

The initial parameters for the FEMU-UF analysis are given in Table 5. The initial displacement residuals for the load-controlled test are significantly lower (*i.e.*, 1.2) when compared with the hybrid test. This fact results from the inability to identify the Poisson's ratio for the hybrid test. From the

Table 4: Standard uncertainties for fully load-controlled and hybrid snail tests

| Control mode | $\gamma_u$ (pixel) | $\gamma_F$ (N) |
|---|---|---|
| Load | 0.012 | 3 |
| Hybrid | 0.020 | 4 |

load-controlled experiment, FEMU-UF identifies $\nu$ (Table 5) whose level corresponds to that obtained when using uniaxial test data.

Table 5: Initial and identified elastic parameters for snail tests

| | $E$ (GPa) | $\nu$ | $\chi_u$ | $\chi_F$ |
|---|---|---|---|---|
| Load controlled snail test | | | | |
| Reference | 158 | 0.28 | 1.18 | 430 |
| FEMU-UF | 157.8±1 | 0.276±0.0004 | 1.15 | 390 |
| Hybrid snail test | | | | |
| Reference | 158 | 0.28 | 2.8 | 420 |
| FEMU-UF | 155±1 | 0.04±0.0006 | 2.7 | 410 |

The identification of the Young's modulus yields for the two cases approximately the same value and induces small decreases of the force residuals. The load-controlled experiment leads to lower values of $\chi_F$ with respect to the hybrid case. The sum of reaction forces obtained from initial and identified values are shown in Figure 14. For the load-controlled test bigger differences are noted for the second loading axis (Figure 14), even for the first loading step (*i.e.*, $F_2 = 0$ a linear increase is observed up to 1.5 kN). This phe-

nomenon may be due to damage (*i.e.,* debonding between the matrix and the nodules) since it was detected in early loading stages by tomography [11]. The second reason can be caused by control errors since the force fluctuations captured on the FE model with the first 10 images are very high (*i.e.,* as high as 0.6 kN). When observing the force response for the hybrid test the same phenomena occur in direction 1.

### *6.2. Identification of plastic parameters*

Yielding of the material stressed biaxially is investigated in the sequel. The two material models describing isotropic and kinematic hardening are analyzed. The displacement (*i.e.,* $\chi_u$) and force (*i.e.,* $\chi_F$) residuals for the two models provide an information on which law describes best the behavior of the material under snail loading regimes. The load-controlled test case consists of 897 acquisitions and the hybrid test of 354 images. The parameters determined from the uniaxial experiment [11] are again introduced as initial parameters for the two material models.

#### *6.2.1. Ludwik's parameters*

The identified parameters (yield stress $\sigma_y$, hardening modulus $K$, and hardening exponent $n$) for the two snail tests are reported in Table 6. For both tests similar values of the parameters are obtained. When compared with the reference parameters it is to be noted that the yield stress $\sigma_y$ and $n$ change equally for both test cases. Namely, $\sigma_y$ increases by 10 % and $n$ decreases for 20 %. The biggest difference is observed for the hardening modulus $K$ for the load-controlled test, it decreases by 300 MPa. However, for hybrid test it increases slightly (*i.e.,* 13 MPa). The identified parameters

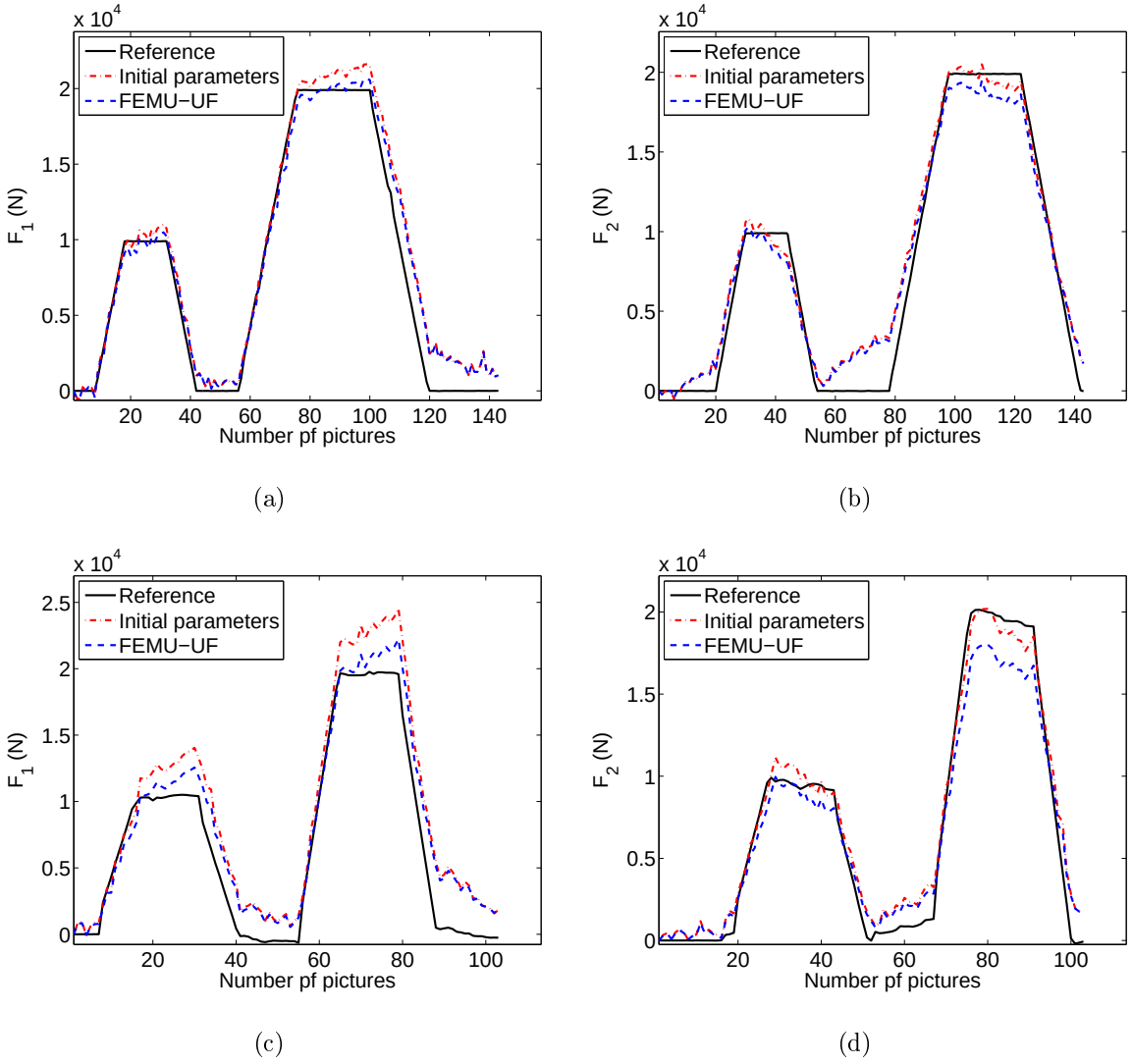


Figure 14: Comparison of measured force and sum of reaction forces computed with the initial and identified elastic parameters for (a-c) loading direction 1, and (b-d) loading direction 2 of the load-controlled (a-b) and hybrid (c-d) snail tests

for both experiments slightly change the displacement and load residuals.

Table 6: Identified Ludwik material parameters on snail test cases

| | $E$ (GPa) | $\nu$ | $\sigma_Y$ (MPa) | $K$ (MPa) | $n$ | $\chi_u$ | $\chi_F$ |
|---|---|---|---|---|---|---|---|
| Load controlled snail test | | | | | | | |
| Reference | 157 | 0.276 | 207 | 1300 | 0.44 | 9.2 | 2200 |
| FEMU-UF | 157 | 0.276 | 230±2 | 1028±2 | 0.36±0.0004 | 8.6 | 2110 |
| Hybrid controlled snail test | | | | | | | |
| Reference | 155 | 0.28 | 207 | 1300 | 0.44 | 23.9 | 1700 |
| FEMU-UF | 155 | 0.28 | 226±2 | 1312±2 | 0.37±0.001 | 23.4 | 1310 |

Figure 15 shows the sum of reaction forces for the two loading directions when the initial and identified parameters are used to describe Ludwik's law. For the load-controlled snail test it is noted that the calculated forces in direction 1 (Figure 15(a)) do not properly capture the measured load levels in the unloading parts while in direction 2 (see Figure 15(b)) no agreement is observed in both loading and unloading parts. In the parts of the loading history where the force level should be constant a significant disagreement is observed.

The same trend is obtained for the hybrid test (see Figure 15(c,d)). Force residuals decrease more in the last test but their levels are very high. When compared with the equibiaxial loading the level of $\chi_F$ is more than two times higher (see Table 2). This information leads to the conclusion that more complex cyclic biaxial loading regimes cannot be described in a reasonable

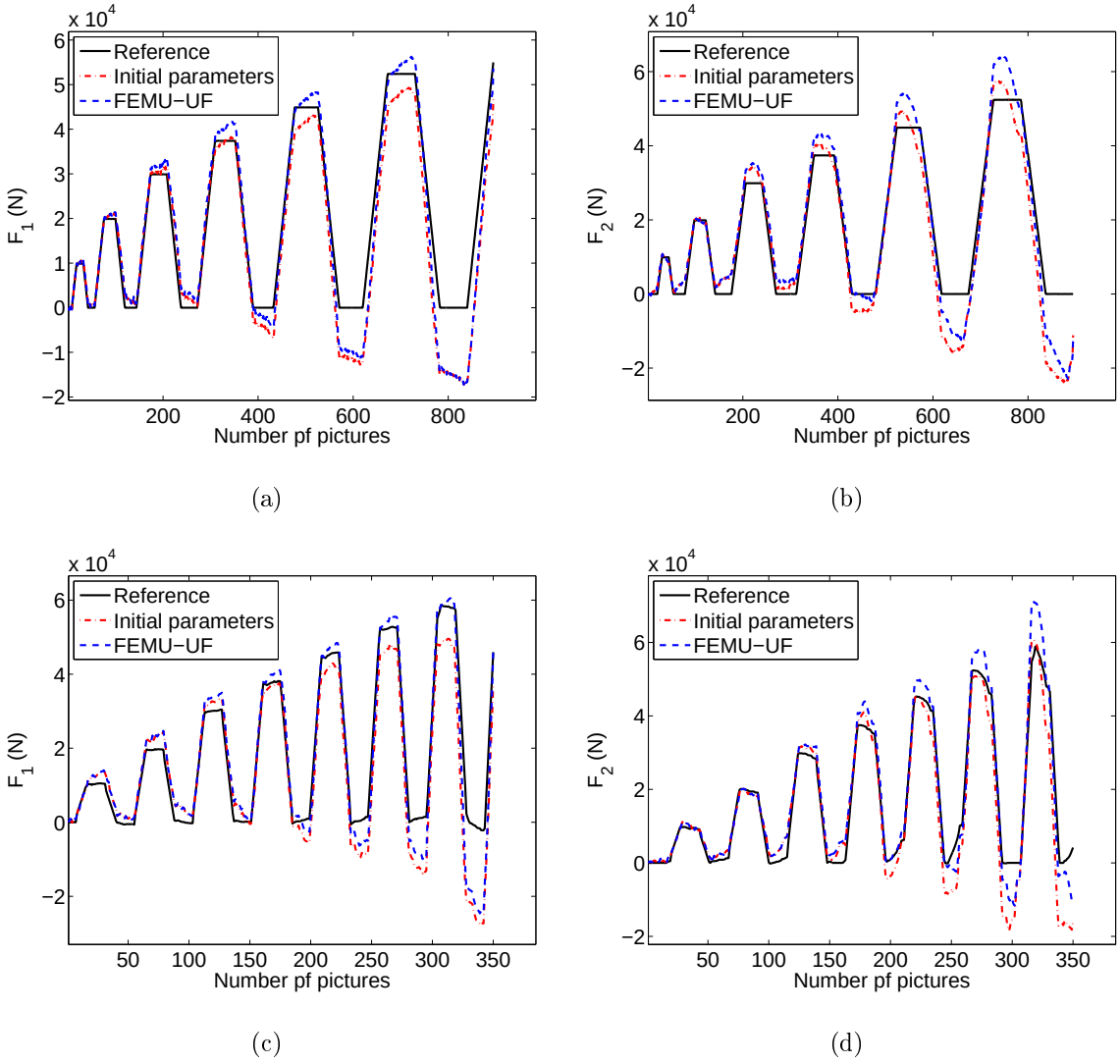


Figure 15: Comparison of measured force and sum of reaction forces computed with the initial and identified material parameters for Ludwik's law for (a-c) loading direction 1, and (b-d) loading direction 2 of the load-controlled (a-b) and hybrid (c-d) snail tests

way with isotropic hardening laws. Hence kinematic hardening will be investigated. It is noted that the displacement residuals are high when compared to the equibiaxial case (see Table 2). $\chi_u$ equals 8.6 for the load-controlled snail test, which makes it 3 times higher than the equibiaxial one. An even bigger difference is reported for the hybrid loaded test (*i.e.,* approximately 12 times higher). It is necessary to emphasize that the strain levels in the snail experiments are higher than in the proportional loading regime, which may explain the increase of $\chi_u$. Hence, it is concluded that the crack network may be more developed. Since the FE model does not capture that phenomenon, it can induce bigger differences between the measured and calculated fields.

*6.2.2. Armstrong-Frederick's parameters*

The initial and identified parameters with the corresponding displacement and force residuals are given in Table 7. The sought parameters (yield stress $\sigma_y$, hardening modulus $C$ and inverse strain $\gamma$) are determined via FEMU-UF while the elastic properties were fixed. The identified yield stress stays unchanged for the load-controlled test and for the hybrid test decreases by 13 MPa. The other two parameters differ more for the two tests. The fully load-controlled test yields a hardening modulus of 57 GPa in comparison with 82 GPa for the hybrid test. The parameter $\gamma$ significantly changes for both snail loading pats. For the load-controlled test it changes for 50 % when compared with the uniaxial experiment (*i.e.,* reference parameters) while for hybrid test it increases by 100 %.

The identified parameters for the two snail experiments yield a significant decrease of the force residuals by more than 50 % when compared with the levels induced by the initial parameters. The best fit of the sought parameters

Table 7: Identified Armstrong-Frederick's parameters for the two snail tests

| | $E$ (GPa) | $\nu$ | $\sigma_Y$ (MPa) | $C$ (GPa) | $\gamma$ | $\chi_u$ | $\chi_F$ |
|---|---|---|---|---|---|---|---|
| Load-controlled snail test | | | | | | | |
| Reference | 157 | 0.276 | 222 | 27 | 107 | 6.9 | 1610 |
| FEMU-UF | 157 | 0.276 | 225±0.1 | 57±0.1 | 158±0.4 | 5.5 | 770 |
| Hybrid snail test | | | | | | | |
| Reference | 155 | 0.28 | 222 | 27 | 107 | 23.5 | 1580 |
| FEMU-UF | 155 | 0.28 | 209±0.2 | 82±0.1 | 212±0.5 | 23.4 | 680 |

is for the load-controlled test, which results in a drop of the displacement residual by 25 % while a lot less for the hybrid experiment (*i.e.,* changes of 0.2 are observed in both cases). However, two times less images are used in the hybrid test, which may explain a part of the differences [20]. On the contrary, the level of $\chi_F$ for the load-controlled case is close to the hybrid test. The level of $\chi_F$ (*i.e.,* 770 and 680) is of the same order of magnitude when compared with the equibiaxial test (*i.e.,* 450). These force residuals are partly attributed to the monitored damage initiations (*i.e.,* debonding between the matrix and graphite nodules [11]) and the subsequently formed crack network (see Appendix B and Appendix C).

To confirm this last statement, the displacement and load residuals are computed for the same set of material parameters once the last loading/unloading cycle has been removed from the analysis. The displacement residuals are virtually identical, which is to be expected because of the way

the boundary conditions are prescribed. Conversely, the load residuals are significantly reduced.

Table 8: Analysis of the load-controlled snail test without taking into account the last loading cycle

| | $E$ (GPa) | $\nu$ | $\sigma_Y$ (MPa) | $C$ (GPa) | $\gamma$ | $\chi_u$ | $\chi_F$ |
|---|---|---|---|---|---|---|---|
| FEMU-UF | 157 | 0.276 | 225 | 57 | 158 | 5.3 | 660 |

Figure 16 shows the calculated reaction forces for the two load histories in order to compare the measured and identified load levels. A better agreement is achieved between the measured and identified sum of reaction forces for both cases when compared with Ludwik's model. However, there is a clear difference with the reference parameters that shows that the identification with a uniaxial test does not describe the snail loading regimes in a reliable way.

### *6.3. Discussion*

Various sets of the sought parameters describing isotropic or kinematic hardening are obtained for the three proposed biaxial loading paths. They differ from those found for the cyclic uniaxial experiment conducted on the same material [11]. The highest force residuals are reported for the load-controlled snail test (see Tables 6 and 7). This leads to the conclusion that increasing the level of loading complexity yields higher discrepancy between the computed and experimental data.

The goal of this section is to observe the modeling error for the uniaxial

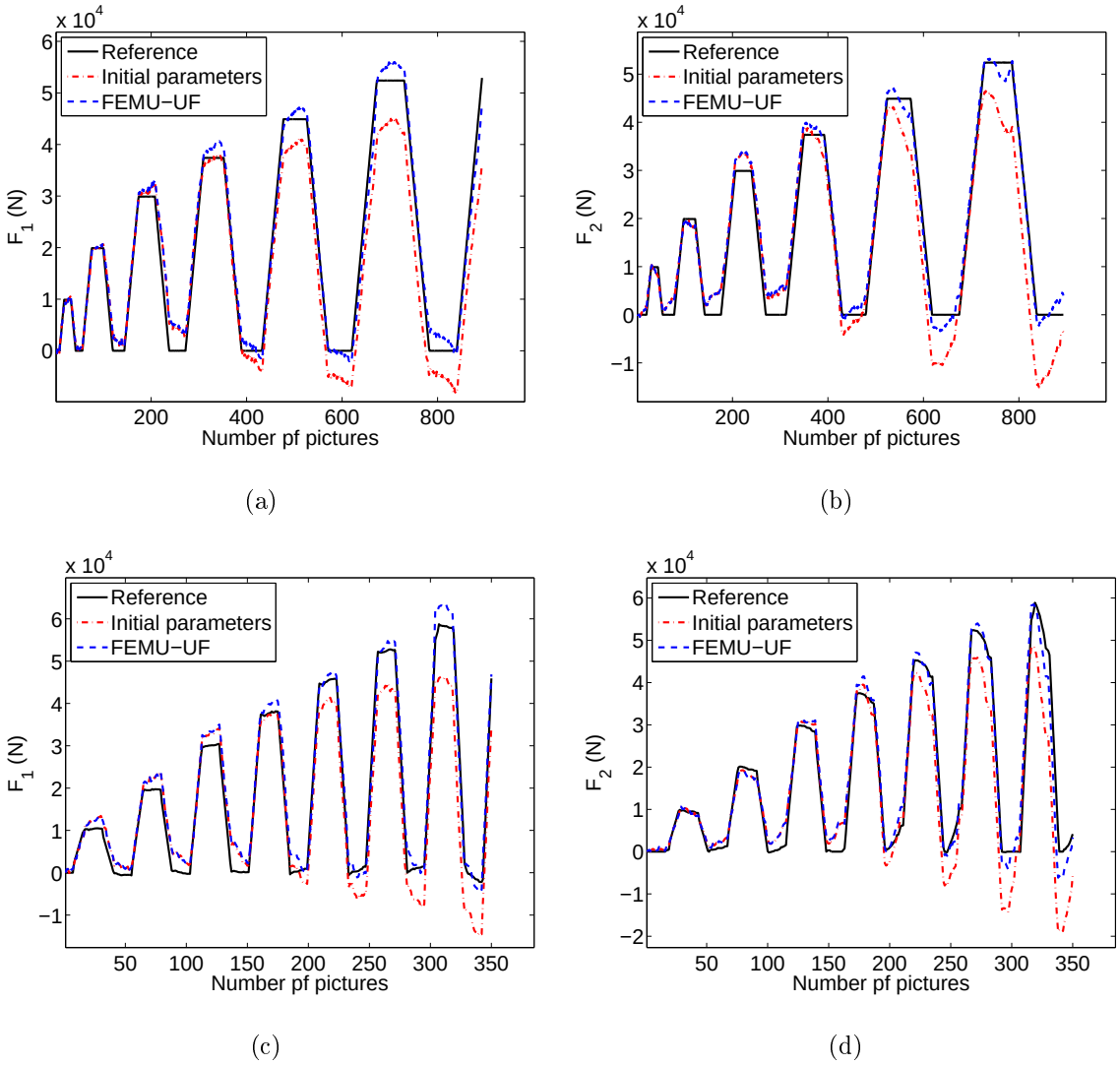


Figure 16: Comparison of measured force and sum of reaction forces computed with the initial and identified material parameters for Armstrong-Frederick's law for (a-c) loading direction 1, and (b-d) loading direction 2 of the load-controlled (a-b) and hybrid (c-d) snail tests

and equibiaxial loading regimes when the parameters determined from the load-controlled snail loading path (Tables 6 and 7) are chosen. The displacement and force residuals are reported in Table 9.

Table 9: Displacement and load residuals for uniaxial and equibiaxial experiment using the identified parameters for the load-controlled snail test

| Loading path | $\chi_u$ | $\chi_F$ |
|---|---|---|
| Ludwik's hardening model | | |
| Uniaxial | 38 | 330 |
| Equibiaxial | 2.3 | 780 |
| Snail | 8.6 | 2110 |
| Armstrong-Frederick's hardening model | | |
| Uniaxial | 40 | 570 |
| Equibiaxial | 1.8 | 580 |
| Snail | 5.5 | 770 |

For both hardening postulates uniaxial and equibiaxial loading regimes yield lower force residuals than those obtained for snail loading history. The highest displacement residuals are reported for the uniaxial test since it has the lowest standard displacement resolution (*i.e.,* 0.004 pixel). The displacement residuals are very close for both models. Conversely, the force residuals are lower on average if the material behavior is described with Armstrong-Frederick's model. Ludwik's model would be equivalent to Armstrong-Frederick's law if uniaxial and equibiaxial tests are solely compared. This last result shows that the snail test is more discriminating test than an equibiaxial

test.

## 7. Conclusion

The objective of the present paper was to study the mechanical properties of SG cast iron under biaxial loading configurations. Two different loading histories were applied in order to study the material response under proportional (*i.e.,* equibiaxial) and nonproportional (*i.e.,* snail) loading regimes. Strain histories were extracted from the measured displacement fields. An equibiaxial loading regime leads to the same strain history for the components measured in the loading direction and the eigen strains. Conversely, snail histories are more complex.

The identification of elastoplastic parameters via FEMU has been performed for the two loading histories when coupling 2D-DIC and 3D-FE analyses. Results obtained from uniaxial experiments were used as inputs to the FEMU-UF procedure. Both elastic parameters were only identified on the snail experiment. One of the reasons is related to the fact that the FE model had just four radii treated as traction-free edges while on 90 % of the boundary nodal displacements were prescribed. The lack of free boundary and the feature of the load history leads to the inability of identifying Poisson's ratio from equibiaxial and hybrid snail tests. When identifiable, the value of the Poisson's ratio is in good agreement with that identified from a uniaxial experiment.

The identification of isotropic (*i.e.,* Ludwik model) and kinematic (*i.e.,* Armstrong-Frederick model) hardening parameters was performed on the whole series of images for the three tests. The identified parameters

yielded higher force residuals than those observed in uniaxial experiments. This can be explained by early damage inception (*i.e.,* in the elastic domain) as detected in a uniaxial test [11] via X-ray tomography. Another reason is associated with model errors as a full 3D-FE analysis is run and only 2D-DIC measurements are used. In the biaxial experiments another phenomenon was reported. Cracks were observed on the strain fields (see Appendix B and Appendix C), which cause higher values of the force residuals. The results obtained with Armstrong-Frederick's model are better than those with Ludwik's isotropic hardening, especially for the snail loading histories. Higher force residuals obtained in the snail experiments when compared with the equibiaxial and uniaxial tests show that the former is more complex and also more discriminating for the investigated models (*i.e.,* Armstrong-Frederick's model outperforms Ludwik's law). It is also expected that non-proportional loading regimes are more damaging, and that other constitutive models (*e.g.,* accounting for damage) need to be considered.

**Acknowledgments**

This work has benefited from a grant from Région Île-de-France (plateforme francilienne d'expérimentation mécanique de troisième génération). ZT thanks Campus France that supported his stay at LMT through an Eiffel scholarship. The authors would also like to warmly thank Dr. Stéphane Roux for numerous discussions on issues introduced in the present paper.

## Appendix A. Investigated constitutive laws

The constitutive laws calibrated herein combine isotropic elasticity with either Ludwik's isotropic hardening, or Armstrong-Frederick's kinematic hardening:

- *Linear isotropic elasticity*

  Before identifying the nonlinear material parameters it was necessary to tune the elastic parameters (*i.e.,* Poisson' ratio $\nu$ and Young's modulus $E$).

- *Ludwik's isotropic hardening*

  Ludwik's law [17] is considered for describing isotropic hardening. Its general expression is

  $$\sigma_{eq} = \sigma_y + Kp^n \tag{A.1}$$

  where the sought parameters are the yield stress $\sigma_y$, the hardening modulus $K$ and the hardening exponent $n$. $\sigma_{eq} = \sqrt{\frac{2}{3}\sigma_{ij}^D\sigma_{ij}^D}$ corresponds to von Mises' equivalent stress, $\sigma_{ij}^D$ the deviatoric stress tensor, and $p$ the cumulated plastic strain.

- *Armstrong-Frederick's kinematic hardening*

  Armstrong and Frederick's model [18] is an upgraded version of Prager's linear kinematic law [21] in which a memory term is added

  $$\dot{\mathbf{X}} = C\dot{\varepsilon}_{pl} + \gamma\mathbf{X}\dot{p} \tag{A.2}$$

  where $\mathbf{X}$ is the back-stress tensor, $C$ and $\gamma$ are material parameters to be identified in addition to the yield stress $\sigma_y$, and $\dot{p}$ the rate of cumulated plastic strain.

## Appendix B. Strain distribution for equibiaxial loading path

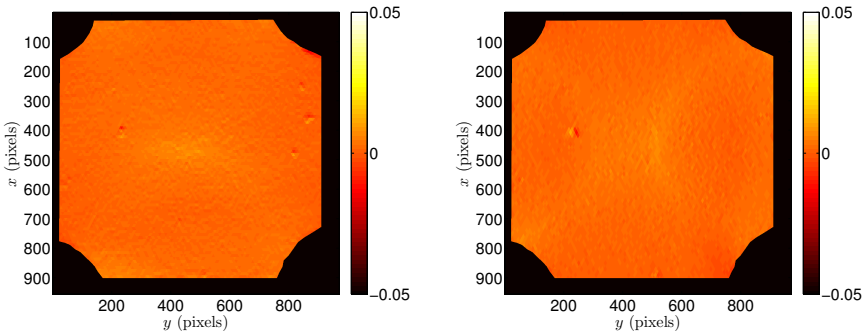


(a) $F_1 = 45$ kN




(b) $F_2 = 45$ kN

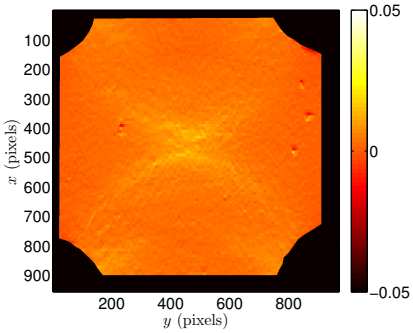


(c) $F_1 = 53$ kN

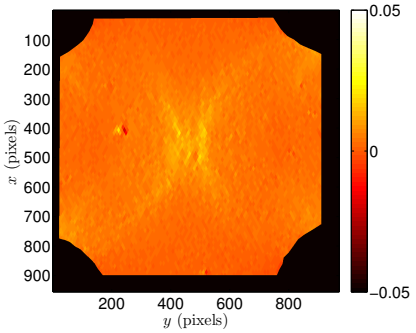


(d) $F_2 = 53$ kN

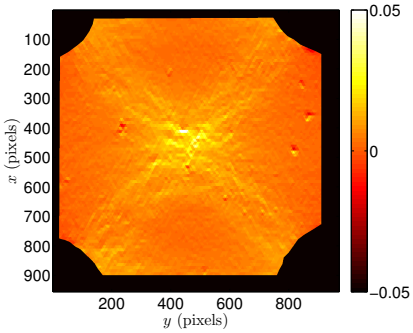


(e) $F_1 = 59$ kN

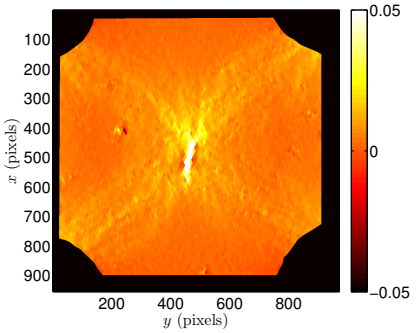


(f) $F_2 = 59$ kN

Figure B.17: Measured normal strain fields for the equibiaxial loading path in the horizontal (left) and vertical (right) directions for a maximum loading level of (a) and (b) 45 kN, (c) and (d) 53 kN, (e) and (f) 59 kN

## Appendix C. Strain distribution for snail loading path

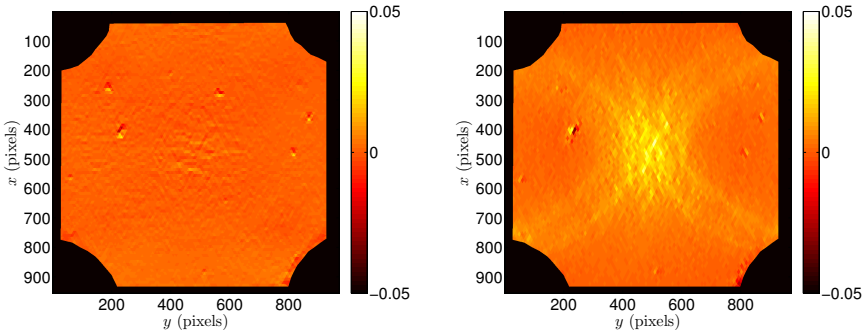


(a) $F_1 = 45$ kN




(b) $F_2 = 45$ kN

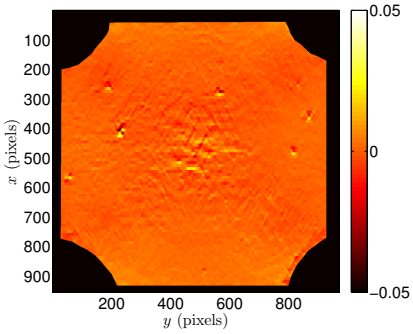


(c) $F_1 = 53$ kN

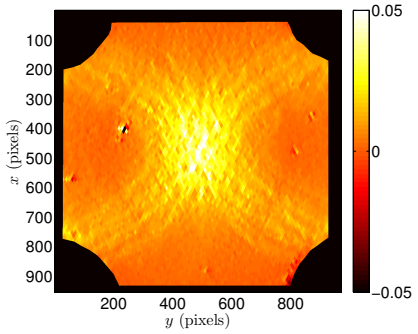


(d) $F_2 = 53$ kN

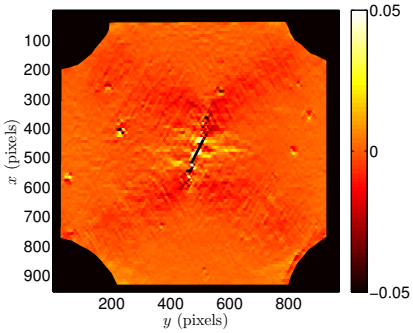


(e) $F_1 = 0$ kN

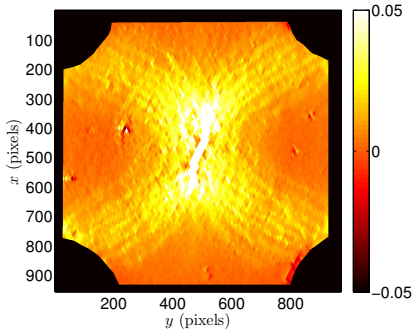


(f) $F_2 = 59$ kN

Figure C.18: Measured strain fields for snail loading path in the horizontal (left) and vertical (right) directions for a maximum loading level of (a) and (b) 45 kN, (c) and (d) 53 kN, (e) and (f) correspond to loading point of 59 kN in the horizontal direction

[1] Batisse, R., Fant-Jaeckels, H. D., Curie, F., and Virely, J. M. Biaxial high cycle fatigue tests on a gas transmission pipeline steel. *Fatigue and Fracture of Engineering Materials and Structures* 1996; **19**(10):1231–1238.

[2] Poncelet, M., Barbier, G., Raka, B., Courtin, S., Desmorat, R., Le-Roux, J., and Vincent, L. Biaxial high cycle fatigue of a type 304l stainless steel: Cyclic strains and crack initiation detection by digital image correlation. *European Journal of Mechanics - A/Solids* 2010; **29**(5):810 – 825.

[3] Fremy, F., Pommier, S., Poncelet, M., Raka, B., Galenne, E., Courtin, S., and Roux, J.-C. L. Load path effect on fatigue crack propagation in I; II; III mixed mode conditions – part 1: Experimental investigations. *International Journal of Fatigue* 2014; **62**(0):104 – 112.

[4] Lecompte, D., Smits A., Sol H., Vantomme J., Van Hemelrijck, D. Mixed numerical-experimental technique for orthotropic parameter identification using biaxial tensile tests on cruciform specimens. *International Journal of Solids and Structures* 2007; **44**(5):1643–1656.

[5] Avril, S., Bonnet, M., Bretelle, A.-S., Grédiac, M., Hild, F., Ienny, P., Latourte, F., Lemosse, D., Pagano, S., Pagnacco, E., and Pierron, F. Overview of identification methods of mechanical parameters based on full-field measurements. *Experimental Mechanics* 2008; **48**(4):381–402.

[6] Cooreman, S., Lecompte, D., Sol, H., Vantomme, J., Debruyne, D. Iden-

tification of Mechanical Material Behavior Through Inverse Modeling and DIC. *Experimental Mechanics* 2008; **48**(4):421–433.

[7] Rossi, M., Pierron, F. Identification of plastic constitutive parameters at large deformations from three dimensional displacement fields. *Computational Mechanics* 2012; **49**(1): 53–71.

[8] Réthoré, J., Muhibullah, Elguedj, T., Coret, M., Chaudet, P., and Combescure, A. Robust identification of elasto-plastic constitutive law parameters from digital images using 3D kinematics. *International Journal of Solids and Structures* 2013; **50**(1):73–85.

[9] Leclerc H, Périé J-N, Roux S, Hild F. Integrated digital image correlation for the identification of mechanical properties. *MIRAGE 2009*, Gagalowicz A, Philips W, eds. Springer: Berlin, 2009; 161-171.

[10] Hild, F. and Roux, S. Comparison of local and global approaches to digital image correlation. *Experimental Mechanics* 2012; **52**(9):1503-1519.

[11] Tomičević, Z., Kodvanj, J., Hild, F. Characterization of nonlinear material behaviour on graphite cast iron via inverse identification methods. Analysis of uniaxial tests. *European Journal of Mechanics - A/Solids* 2015; *submitted.*

[12] Sermage, J., Lemaitre, J., and Desmorat, R. Multiaxial creep-fatigue under anisothermal conditions. *Fatigue & Fracture of Engineering Materials & Structures* 2000; **23**:241-252.

[13] Doudard, C., Poncelet, M., Calloch, S., Boue, C., Hild, F., and Galtier, A. Determination of an HCF criterion by thermal measurements under biaxial cyclic loading. *International Journal of Fatigue* 2007; **29**(4):748 – 757.

[14] Lemaitre, J., Sermage, J.-P., and Desmorat, R. A two scale damage concept applied to fatigue. *International Journal of Fracture* 1999; **97**:67–81.

[15] Tomičević, Z., Hild, F., and Roux, S. Mechanics-aided digital image correlation. *Journal of Strain Analysis for Engineering Design* 2013; **48**(5):330–343.

[16] Mathieu, F., Leclerc, H., Hild, F., and Roux, S. Estimation of elastoplastic parameters via weighted FEMU and integrated-DIC. *Experimental Mechanics* 2015; **55**(1):105–119.

[17] Ludwik, P. *Elemente der technologischen Mechanik.* Verlag von Julius Springer 1909; Berlin.

[18] Armstrong, P. and Frederick, C. A mathematical representation of the multiaxial bauschinger effect. *Report RD/B/N 731, Central Electricity Generating Board* 1966.

[19] Gras, R., Leclerc, H., Hild, F., Roux, S., and Schneider, J. Identification of a set of macroscopic elastic parameters in a 3D woven composite: Uncertainty analysis and regularization. *International Journal of Solids & Structures* 2015; **55**: 2–16.

[20] Robert, L., Velay, V., Decultot, N., and Ramde, S. Identification of hardening parameters using finite element models and full-field measurements: some case studies. *The Journal of Strain Analysis for Engineering Design* 2012; **47**(1):3–17.

[21] Prager, W. A new method of analysing stress and strain in work hardening plastic solids. *ASME Journal of Applied Mechanics* 1956; **78**(493).

## List of Figures

## List of Tables